3D numerical modelling of turning-induced residual stresses – A two-scale approach based on equivalent thermo-mechanical loadings

Maxime Dumas, Dorian Fabre, Frédéric Valiorgue, Guillaume Kermouche, Alexis van Robaeys, Mathieu Girinon, Alexandre Brosse, Habib Karaouni, Joël Rech

HAL Id: emse-03788474
https://hal-emse.ccsd.cnrs.fr/emse-03788474v1

3D numerical modelling of turning-induced residual stresses - a two-scale approach based on equivalent thermo-mechanical loadings

Highlights

- A new original method to predict residual stress fields induced by a longitudinal turning operation is presented.

- It is a 3D hybrid method that combines basic experimental data (turning forces measurement) and numerical modelling.

- The model predicts residual stresses based on the application of 3D equivalent thermo-mechanical loadings in movement over the 3D surface during several revolutions.

- This hybrid method is an improvement of a previous one. The originality of the new method is related to a finer estimation of the 3D equivalent thermo-mechanical loadings thanks to preliminary simple 2D orthogonal cutting models. Morever the new model takes into account the effective surface toography of the machined surface instead of assuming it as flat in the previous model.

- It provides much more accurate residual stress fields within a reasonable computation duration, that makes it compatible with an industrial use.

Graphical abstract
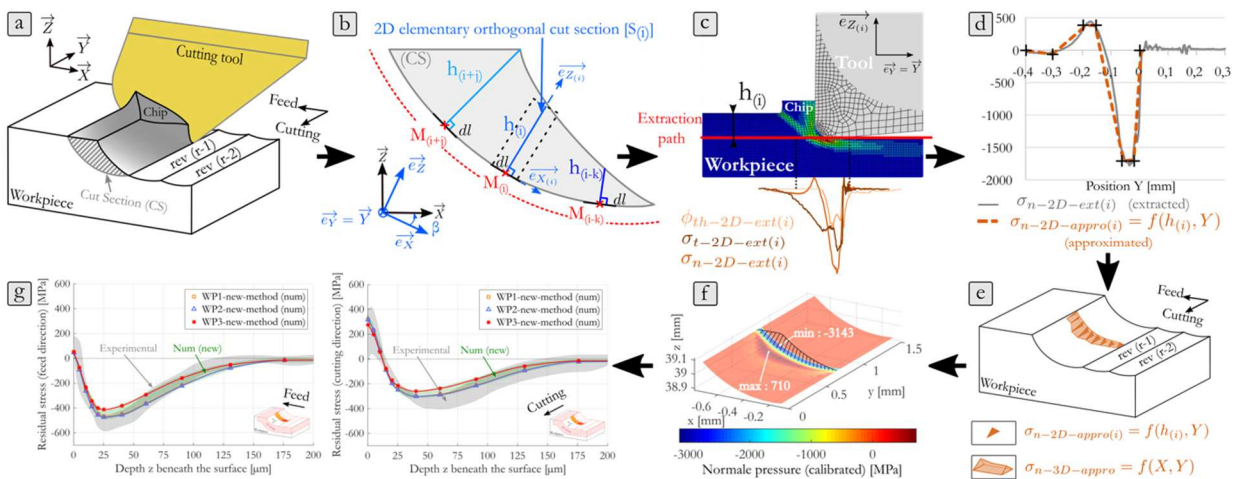
Abstract

Nowadays, fatigue life of engineering components is a major topic. In the literature, extensive works have been reported in order to assess the machining-induced surface integrity which is known to be a first-order parameter for the fatigue resistance. This paper lies in the framework of turning-induced residual stress prediction by presenting an up-dated method based on a two-scale approach. Previous works aimed at building a 3D hybrid method consist of modelling the turning consequences through equivalent thermo-mechanical loadings combining a finite element model with experimental tests. The new proposed global hybrid strategy keeps the same concept but has the advantage of defining the thermo-mechanical shapes more accurately thanks to local 2D orthogonal cutting models. Moreover, the calibration of the equivalent thermo-mechanical loadings is easier as only turning forces have to be measured, which makes it more accessible to end-users. Finally, the model provides results considering the effective machined surface topography instead of considering a basic flat surface. After carefully detailing each step of the numerical method, a validation case study concerning a longitudinal turning operation on a 15-5PH martensitic stainless steel is proposed. By comparing numerical results with experimental residual stresses coming from X-Ray diffraction, the new numerical method shows its superiority to predict, within few hours, much more accuratly the residual stress state induced by a real longitudinal turning operation.

Keywords: turning; residual stress modelling; 3D hybrid method; X-Ray diffraction

1 Introduction

Mechanical industries have to improve the fatigue life of their safety engineering components. Several studies, such as Smith et al. (2007), have shown that fatigue resistance of a surface is determined by its 'surface integrity'. The concept of surface integrity, introduced by Griffith (1971), includes a range of criteria dealing with surface roughness, residual stress and microstructure. The influence of surface integrity on the functional performance and life of machined components has been widely reported by a huge number of papers and summarised by Davim (2008). Among surface integrity criteria, several papers, such as Paulo Davim (2007), reported the significant role that residual stresses play in determining the fatigue life of critical products. Especially, near surface compressive stresses are beneficial for the fatigue life. On the contrary, high tensile residual stresses at the surface may induce much shorter fatigue life as noticed by Guo et al. (2010). Residual stress level depends on the thermo-mechanical loadings induced by all the previous manufacturing operations. However, the last cutting operation has the main responsibility since Guo et al. (2002). This paper focuses on finishing longitudinal turning operations (Fig. 1-a) as they are among the most widely used finishing operations for rotary shafts. The objective of the paper consists in proposing an original 3D numerical model to predict the residual stress state related to this operation.

As far as the state of the art is concerned, a huge number of models have been developed. Historically, 2D analytical models such as those developed by Ulutan and Ozel (2011), were the most popular as they provide rapidly qualitative results with a short time. However, these analytical models have strong assumptions that limits their ability to provide quantitative results. So, several researchers proposed numerical models thanks to the development of computational capabilities. For instance, Shet and Deng (2003) have used a numerical Lagrangian formulation in orthogonal cutting. Such models assume that the cutting operation can be considered as a 2D plain strain configuration, which is far from a 3D industrial longitudinal cutting operation. The second issue comes from the high strain around the cutting edge radius (separation) that leads to mesh distortions as highlighted by Ee et al. (2005). The third issue comes from the weak modelling of friction at the boundaries of two Lagrangian meshed solids in

movement as explained in Liu and Guo (2000). As a consequence, Nasr et al. (2007) have also used 2D Arbitrary Lagrangian Eulerian (A.L.E) formulation to improve mesh distortion and contact modelling issues. Unfortunately, as these works use an explicit time integration algorithm, they lead to difficulties in modelling the relaxation time (crucial for residual stress prediction). Finally, even these 2D models are of scientific interest to understand the mechanisms leading to residual stresses in an orthogonal cutting configuration, the industrial interest is related to 3D surfaces generated by a large number of revolutions (longitudinal turning). Indeed, the cutting tool modifies the residual stress state obtained during the previous revolutions. As shown by Mondelin et al. (2012), several cutting revolutions are necessary to reach a steady state in turning. So, some researchers, such as Attanasio et al. (2009), proposed a 3D Lagrangian formulation to predict residual stresses in cutting. This paper brings a better understanding of the physical phenomena leading to residual stress generation. However, the previous weaknesses of the Lagrangian formulation remain, and the computational time is not realistic for industry.

An alternative approach proposed by Mondelin et al. (2012) consists in modelling the residual stress generation by removing the chip formation and cutting tool modelling and replacing it with equivalent thermo-mechanical loadings (Figs. 1-b,c). These equivalent loadings are moved onto the machined surface with a velocity equal to the cutting speed. After the cooling phase, this model makes residual stress prediction possible. This hybrid model for residual stress prediction, based on an implicit formulation, presents advantages like the absence of highly distorted mesh, the possibility of 3D multi-revolution simulations, and accurate mechanical equilibrium computation. This model has been improved by Mondelin et al. (2012).
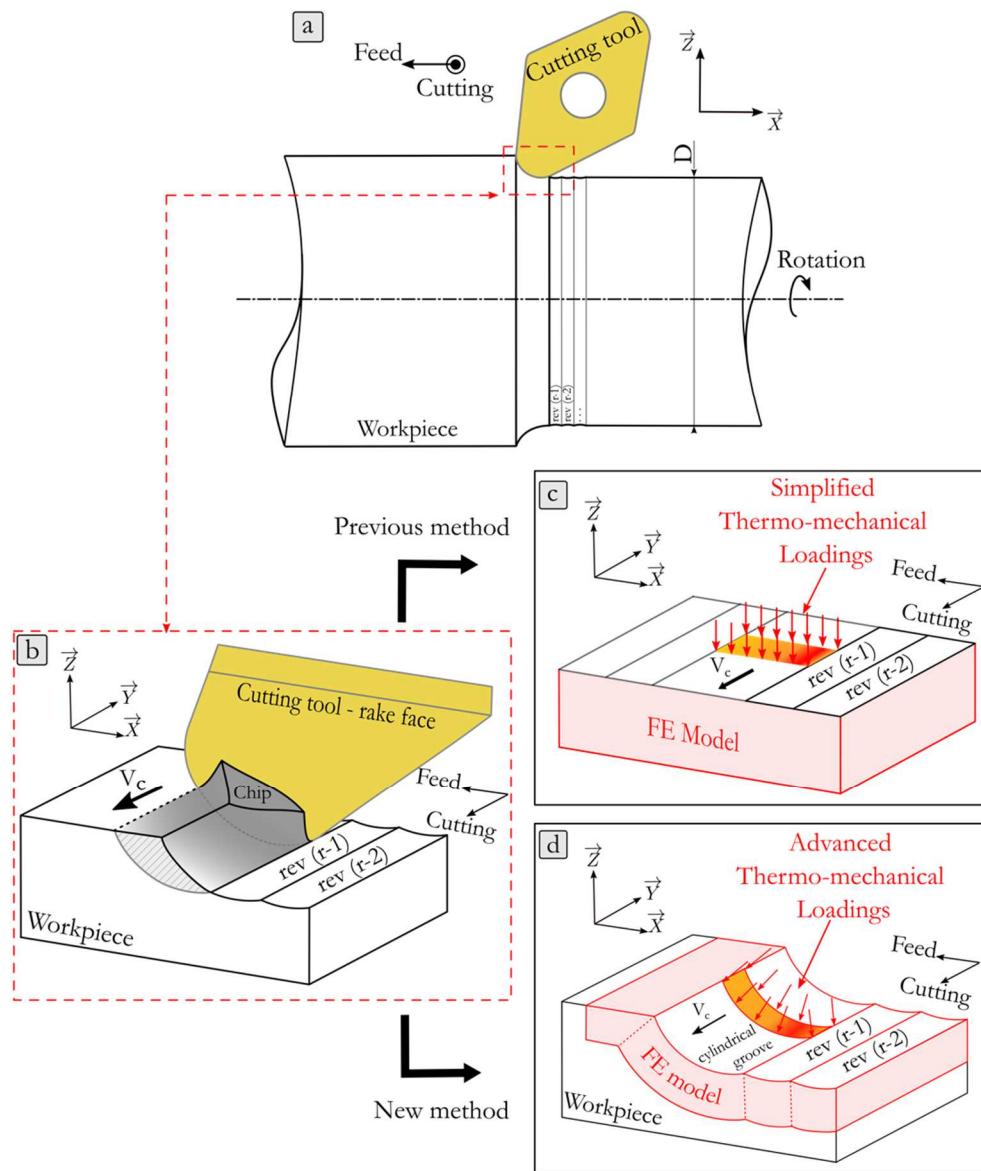
Fig. 1: Principle of the residual stress modelling based on a two-scale approach. a) longitudinal turning operation, b) zoom on the chip formation zone, c) turning operation modelling based on equivalent thermo-mechanical loadings (previous method) (Mondelin et al. (2012)), d) turning operation modelling based on new advanced equivalent thermo-mechanical loadings (new method).

As shown in Fig. 2, in the previous method the thermal and mechanical loadings have simple shapes (a homogeneous or a linear or a parabolic distribution) depending on the area (primary shear zone in front of the cutting tool or third shear zone below the flank face) and depending on the section (YZ) or (XZ). The magnitude of the thermo-mechanical loading is calibrated by means of preliminary experimental tests: friction tests and orthogonal cutting tests as described by Mondelin et al. (2012). The combination of simple thermo-mechanical distributions of loadings with experimental parameters (forces, chip thickness, contact length...) is the origin of its surname: the 3D hybrid model. Finally, the thermo-mechanical loadings are applied and moved onto a flat surface during several revolutions with a shift between each revolution corresponding to the tool feed (Fig. 1-c). A good agreement is obtained between the predicted and analysed residual stress profiles (X-Ray diffraction method) for a finish longitudinal turning operation on a 15-5PH martensitic stainless steel.
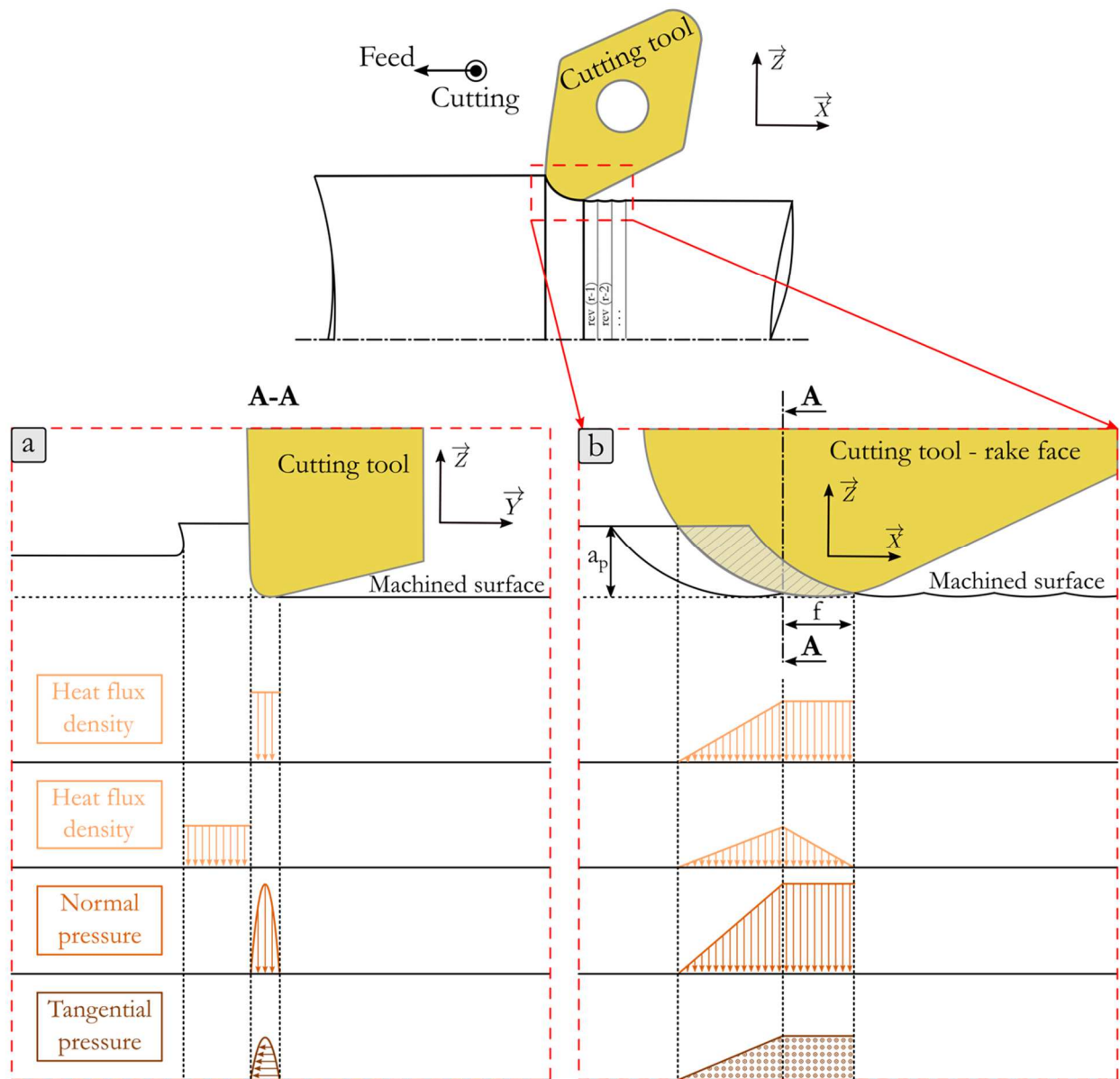
Fig. 2: Simplified loadings shapes description as defined in the conventional hybrid method (Mondelin et al. (2012)): a) shapes in the plan (Y,Z), b) shapes in the plane (X,Z).

However, this method has some weak points that should be improved. First the quantification and distribution of the thermo-mechanical loading could be improved by considering more complex interaction mechanisms. Second, the machined surface is assumed as flat, whereas the effective contact area between the tool and the material is closer to a "cylindrical groove" generated by the movement of the tool tip as shown in Fig. 1-d. So, this paper aims first at improving both quantification and distribution of the thermo-mechanical loadings, and second, to apply it to a more realistic machined surface (cylindrical grooves).
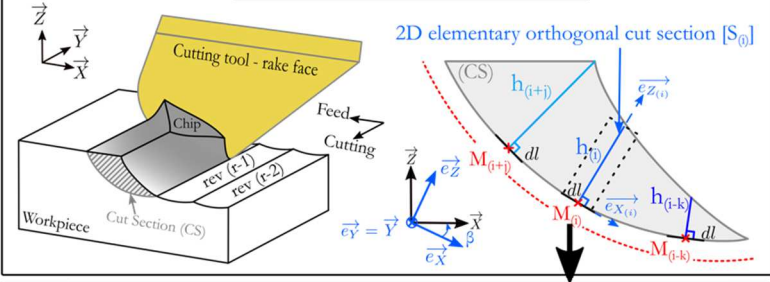
2 Residual stress modelling: a two-scale approach based on advanced equivalent thermo-mechanical loadings

This section aims at presenting the new strategy to predict residual stresses induced in turning. The flowchart presented in Fig. 3 illustrates various steps. Let us begin with a quick overview on the modelling strategy before describing each step in details in the next subsections.
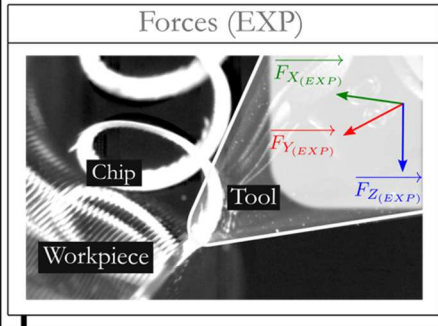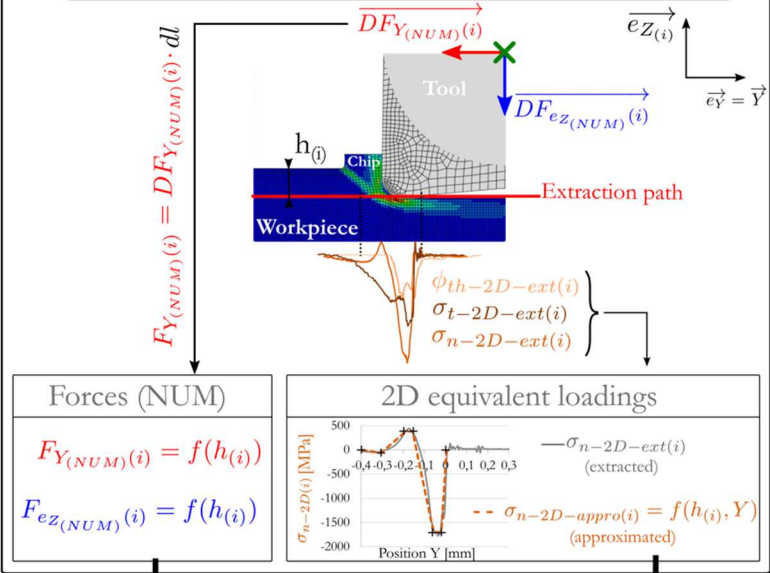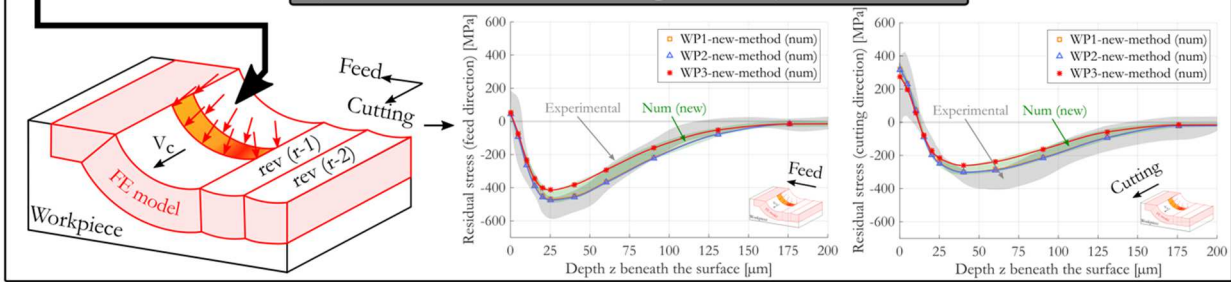
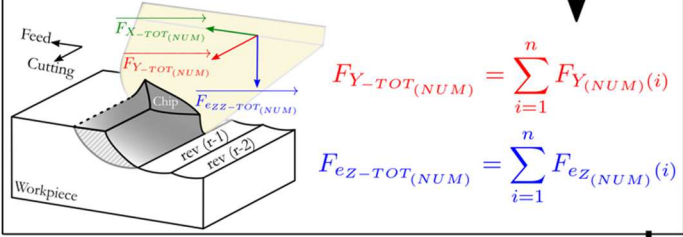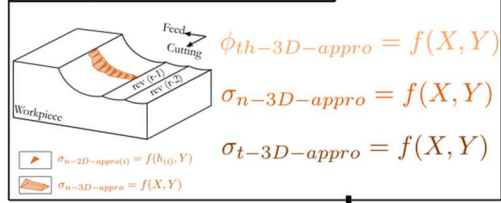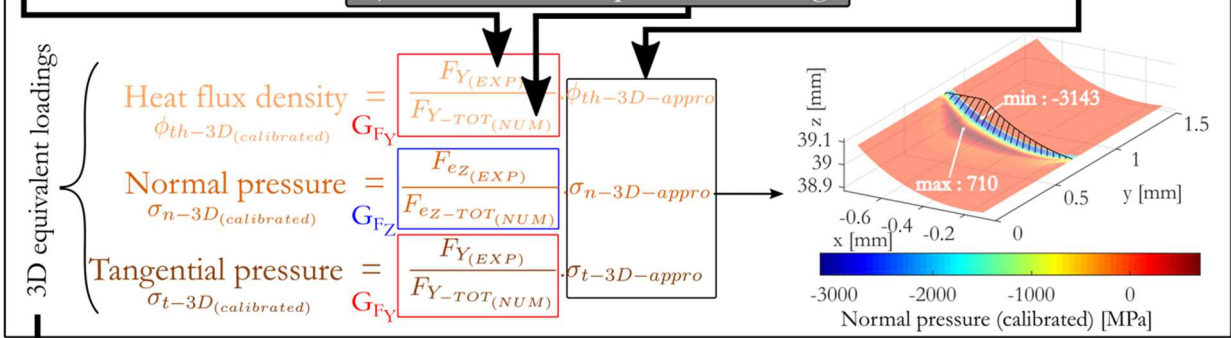**Fig. 3:** Flowchart of the new 3D hybrid methodology through steps number zero to six

Fig. 3-1 describes the geometrical interaction between the cutting tool tip and the workpiece. The cut section, called CS, is divided into several 2D elementary orthogonal sections $S_{(i)}$ having an uncut chip thickness $h_{(i)}$. Then Fig. 3-2 illustrates that a 2D numerical model simulates the material removal for each section $S_{(i)}$. Based on these simulations, the thermo-mechanical loadings induced on the machined surface of each section $S_{(i)}$ are extracted along the line called "extraction path". This provides the 2D density of heat flux $\varphi_{th-2D(i)}$, the normal stress $\sigma_{n-2D(i)}$ and the tangential stress $\sigma_{t-2D(i)}$ along the extraction path. By combining these 2D loadings on the effective cylindrical machined surface (a cylindrical groove), it becomes possible to model the 3D density of heat flux $\varphi_{th-3D-appro}$, normal stress $\sigma_{n-3D-appro}$ and tangential stress $\sigma_{t-3D-appro}$ as shown in Fig. 3-4. Unfortunately, it is well known that ALE 2D numerical simulations do not provide an accurate estimation of the thermo-mechanical loadings. However, it is assumed that the shapes of these loadings are relevant, but not their magnitudes. As this paper is based on a so-called "hybrid approach", this weak point is compensated by the measurement of the experimental cutting force $F_{Y(EXP)}$ and penetration force $F_{Z(EXP)}$ (Fig. 3-0), that are compared to the numerical values of cutting force $F_{Y-TOT(NUM)}$ and penetration force $F_{ez-TOT(NUM)}$. The ratio between measured and numerical values provides two compensation factors (G_{FY} and G_{FZ}) that enable to the calibration of the magnitudes of thermo-mechanical loadings (Fig. 3-5). The 3D thermomechanical loadings are now defined and calibrated. Fig. 3-6 shows the final step consisting of applying the loadings on the machined surface for several revolutions, which leads to the prediction of the residual stress state beneath the surface. Details on each step are provided in the following subsections.

2.1 Geometrical approach

The modelling strategy starts by defining the undeformed cut section CS (Fig. 4-a). The shape of this section CS depends on :

- the cutting conditions (depth of cut a_p, feed f)

- the tool geometry (tool tip radius R_ϵ)

As the model considers a parallelepiped volume of material of some millimetres, the curvature of the effective cylindrical part is not considered. The trajectory of the tool tip is assumed as straight, that generates a cylindrical grooved surface for each revolution. Fig. 4-a illustrates the revolution (r), whereas the remaining machined surface generated by the two previous revolutions ($r-1$) and ($r-2$) are visible. Fig. 4-b focuses on undeformed cut sections CS in the plane (XZ). The cutting edge is discretised with several points $M_{(i)}$, $i = 1$ to p, where p is the number of points where $h_{(i)}$ are located. A section $S_{(i)}$, perpendicular to the cutting edge, is defined as well as its corresponding uncut chip thickness $h_{(i)}$. Two coordinate systems are defined: the main system $S_R = \left(O, \vec{X}, \vec{Y}, \vec{Z}\right)$ is linked to the workpiece whereas the second $S_L = \left(M_{(i)}, \overrightarrow{e_X}, \overrightarrow{e_Y}, \overrightarrow{e_Z}\right)$ is linked to the point $M_{(i)}$ along the cutting edge. The two coordinates systems are inclined with an angle $\beta = \left(\overrightarrow{e_X}, \vec{X}\right)$ that orientates 2D each cut section $S_{(i)}$.
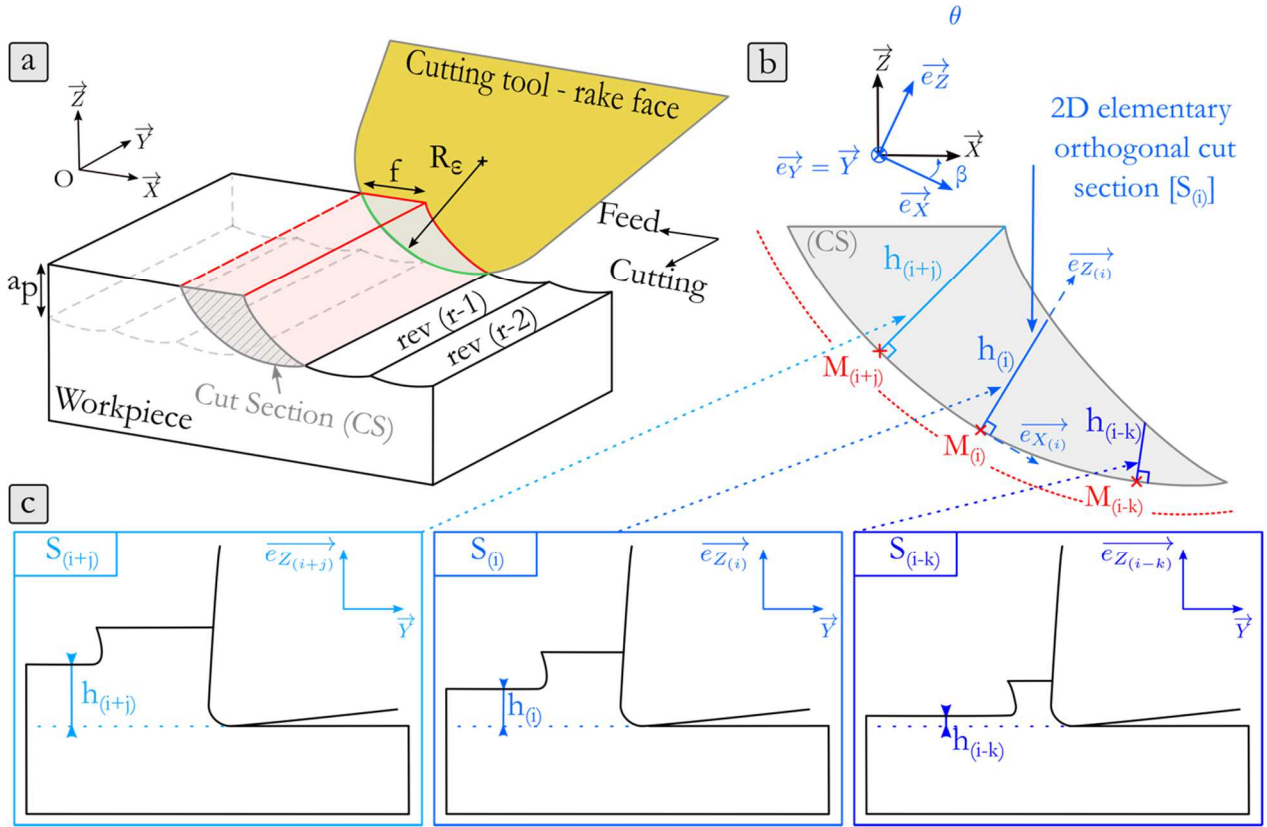
Fig. 4: Geometrical approach to discretise the cutting edge in several 2D elementary orthogonal cut sections. a) material removal description, b) theoretical undeformed cut section CS and 2D sections $S_{(i)}$ parametrisation along the cutting edge, c) example of 2D sections $S_{(i)}$ with the corresponding uncut chip thickness $h_{(i)}$.

Fig. 4-b illustrates that each section $S_{(i)}$ has a different uncut chip thickness $h_{(i)}$. It is assumed that the material removal can be considered as an orthogonal cutting operation (Fig. 4-c). As a consequence, each 2D cut section $S_{(i)}$ is supposed to be independent from its neighbor (plane strain configuration). The orthogonal cut section is described by its uncut chip thickness $h_{(i)}$, and also by its local rake angle $\gamma_{(i)}$, clearance angle $\alpha_{(i)}$, cutting edge radius $R_\beta(i)$ and tool inclination angle $\lambda_{s(i)}$ that may vary along the cutting edge. As this paper presents this new modelling strategy for the first time, the tool micro-geometry is simplified and assumed as constant along the cutting edge. So $\alpha_{(i)}$ = constant = α, $\gamma_{(i)}$ = constant = γ, $R_\beta(i)$ = constant = R_β and $\lambda_{s(i)}$ = constant = λ_s = 0. Only the uncut chip thickness $h_{(i)}$ has a different value according to the chosen point $M_{(i)}$ along the cutting edge.

2.2 Elementary 2D orthogonal cutting - ALE modelling

The second step of the methodology (Fig. 3-2) consists in assessing the impact of the material removal on the machined workpiece for each section $S_{(i)}$. For that purpose, a 2D numerical orthogonal cutting model is used.

2.2.1 2D Orthogonal cutting model

The numerical cutting model has been developed by Courbon et al. (2014) in Abaqus Explicit. It is based on an Arbitrary Lagrangian Eulerian formulation with an adaptive Lagrangian mesh. It is assumed that strains only occur in the plane $(\vec{Y}, \overrightarrow{eZ_{(i)}})$ (Fig. 5). The workpiece and the tool are meshed with CPE4RT elements. The tool is modelled by considering only the thermophysical properties of the carbide

substrate. The coating is not considered because its thickness is too small compared with the scale of the model. Moreover, its thickness makes it transparent as far as heat transfer is concerned. On the contrary, its influence on friction and heat partition at the interface are taken into account. This will be discussed in section 3.2. The tool is considered as rigid and the workpiece as deformable. Two specific refined-mesh partitions are defined to accurately extract the loadings at the tool/surface interface. The mesh size and boundary conditions are presented in Fig. 5. Input data of the model will be discussed in a following section. More details on the numerical model can be found in Courbon et al. (2014).

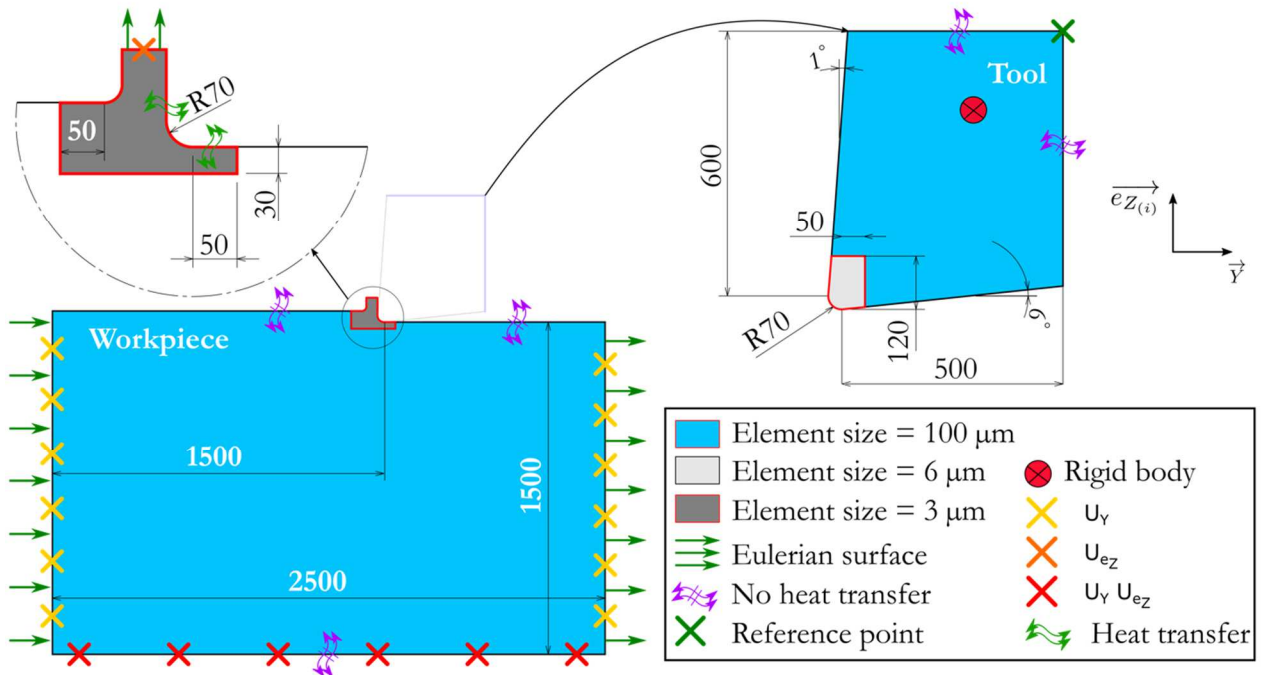**Fig. 5:** 2D Elementary ALE cutting modelling. Description of the used finite element mesh size and distribution as well as boundary conditions.

2.2.2   2D equivalent thermo-mechanical loadings definition

The 2D ALE numerical model is used to simulate material removal phenomena for each cut section $S_{(i)}$ (i.e., each uncut chip thickness $h_{(i)}$) at point $M_{(i)}$.
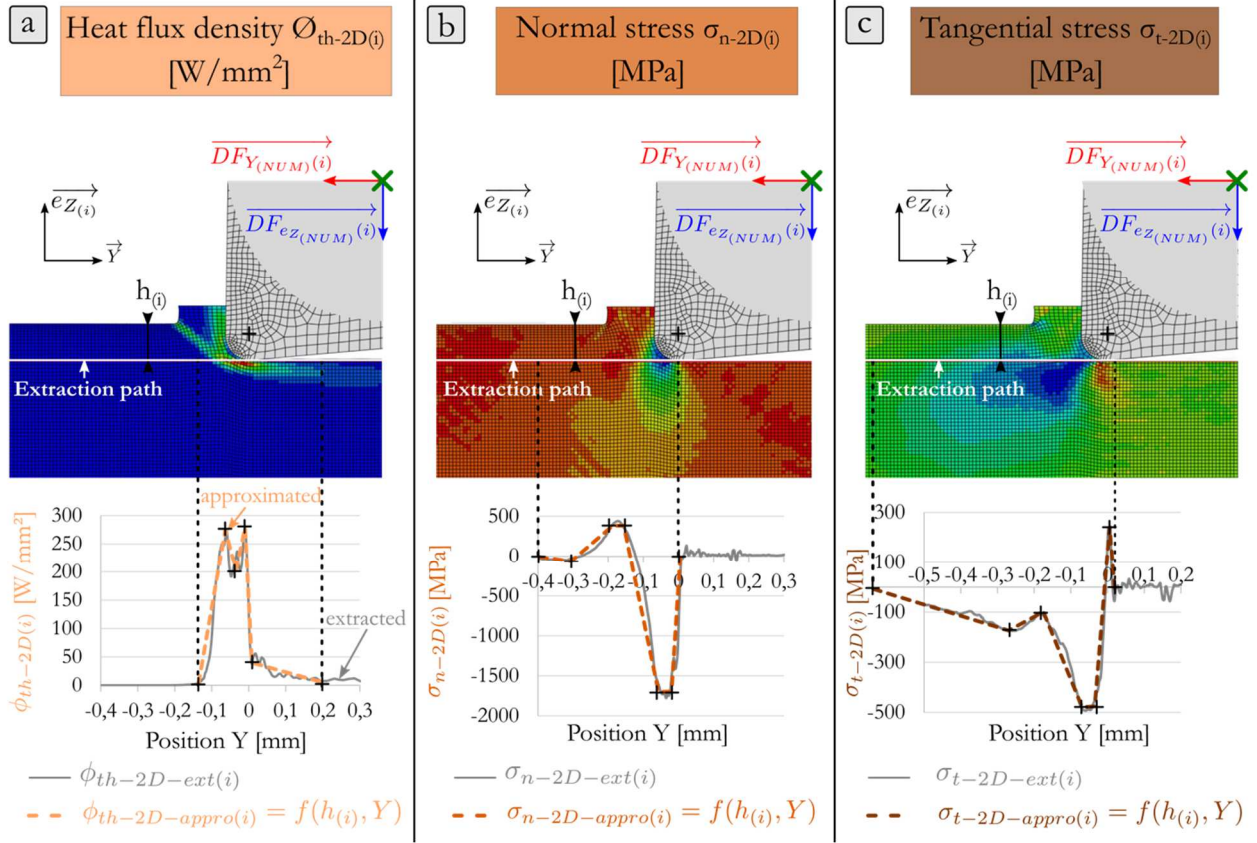
Fig. 6: 2D equivalent loadings and turning forces densities extractions from 2D ALE cutting models. Given an uncut chip thickness $h_{(i)}$ at point $M_{(i)}$ located in the cutting edge and for each considered equivalent loading, linear approximation of the complex extracted shapes, a) heat flux density $\varphi_{th-2D-appro(i)}$, b) normal pressure $\sigma_{n-2D-appro(i)}$, c) tangential pressure $\sigma_{t-2D-appro(i)}$.

Fig. 6 illustrates the heat flux density *HFL* (Fig. 6-a), the normal stress *S*22 parallel to $\overrightarrow{eZ_{(i)}}$ (Fig. 6-b) and the tangential stress *S*12 parallel to *Y* (Fig. 6-c). The previous hybrid model proposed by Mondelin et al. (2012) has shown that the thermo-mechanical loadings supported by the future machined surface can be extracted along the so-called "extraction path": the heat flux density $\varphi_{th-2D-ext(i)}$, normal stress $\sigma_{n-2D-ext(i)}$ and tangential stress $\sigma_{t-2D-ext(i)}$. As these three parameters vary along the extraction path, their shape is rather complex. It has been decided to simplify them with linear sectors as shown in Fig. 6. These simplified thermo-mechanical loadings are called: $\varphi_{th-2D-appro(i)}$ for the heat flux density, $\sigma_{n-2D-appro(i)}$ for the normal stress and $\sigma_{t-2D-appro(i)}$ for the tangential stress. These three densities depend on the uncut chip thickness $h_{(i)}$ and the position along the *Y* axis (see eq. 1 to eq 3).

$$\varphi_{th-2D(i)} = f(h_{(i)}, Y) \tag{1}$$

$$\sigma_{n-2D(i)} = f(h_{(i)}, Y) \tag{2}$$

$$\sigma_{t-2D(i)} = f(h_{(i)}, Y) \tag{3}$$

In addition, elementary macroscopic forces are estimated at the reference point in the tool for each elementary section (Fig. 6): the elementary cutting force $DF_{Y(NUM)}(i)$ and the elementary penetration force $DF_{ez(NUM)}(i)$.

2.3 Approximated 3D equivalent thermo-mechanical loadings building

Based on the thermo-mechanical loadings $\varphi_{th-2D-appro(i)}$, $\sigma_{n-2D-appro(i)}$ and $\sigma_{t-2D-appro(i)}$ for each 2D section $S_{(i)}$, it becomes possible to build the 3D equivalent thermo-mechanical loadings on the cylindrical

groove: $\varphi_{th-3D-appro}$ for the heat flux density, $\sigma_{n-3D-appro}$ for the normal stress, and $\sigma_{t-3D-appro}$ for the tangential stress (step corresponding to Figs. 3-4). These loadings vary for each coordinate (X,Y) on the cylindrical surface. Fig. 7 plots a schematic drawing of the normal stress $\sigma_{n-3D-appro}$ over the groove. As stated previously, it is assumed that each section $S_{(i)}$ does not interact with its neighbours. This assumption should be improved in the future when 3D ALE cutting models will be available.

$$\sigma_{n-2D-appro(i)} = f(h_{(i)}, Y)$$

$$\sigma_{n-3D-appro} = f(X, Y)$$
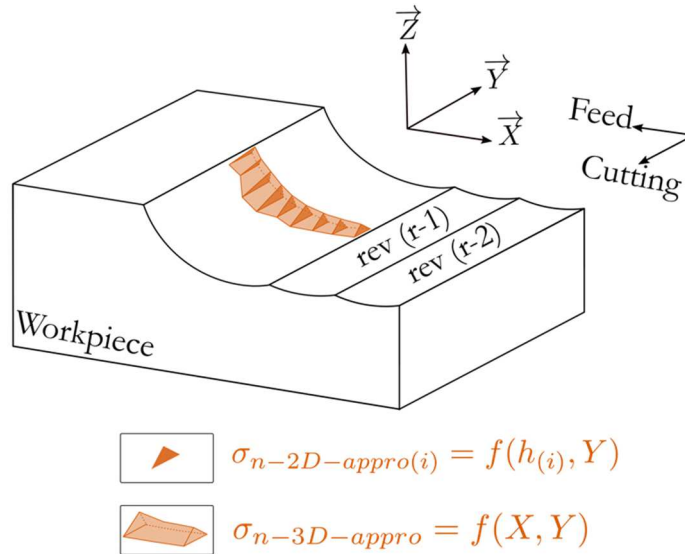
Fig. 7: 3D thermo-mechanical shapes building - example of the normal pressure (see Fig. 6).

At this step, the shape of thermo-mechanical loadings is modelled. However, it is well known that the ALE simulations are not accurate enough. Significant differences between experimental and numerical values are observable. Moreover, cutting and penetration forces are not estimated with the same accuracy. The cutting force F_Y is usually rather well predicted by ALE models. On the contrary, the penetration force is significantly under estimated. This general statement will be confirmed later in the paper in Table 7. So, there is a clear need to modify the 3D thermo-mechanical loadings so as to adjust their magnitude by taking into account the effective cutting force $F_{Y(EXP)}$ and penetration force $F_{Z(EXP)}$ that have been measured during a real longitudinal turning operation (Fig. 3-0) thanks to a Kistler dynamometer. This is the main principle of a so-called "hybrid" model that enables the calibration of the equivalent thermo-mechanical loadings thanks to easily accessible experimental parameters. So, it is necessary to estimate the numerical macroscopic cutting force $F_{Y-TOT(NUM)}$ and penetration force $F_{eZZ-TOT(NUM)}$ applied on the workpiece (step corresponding to Fig. 3-3).
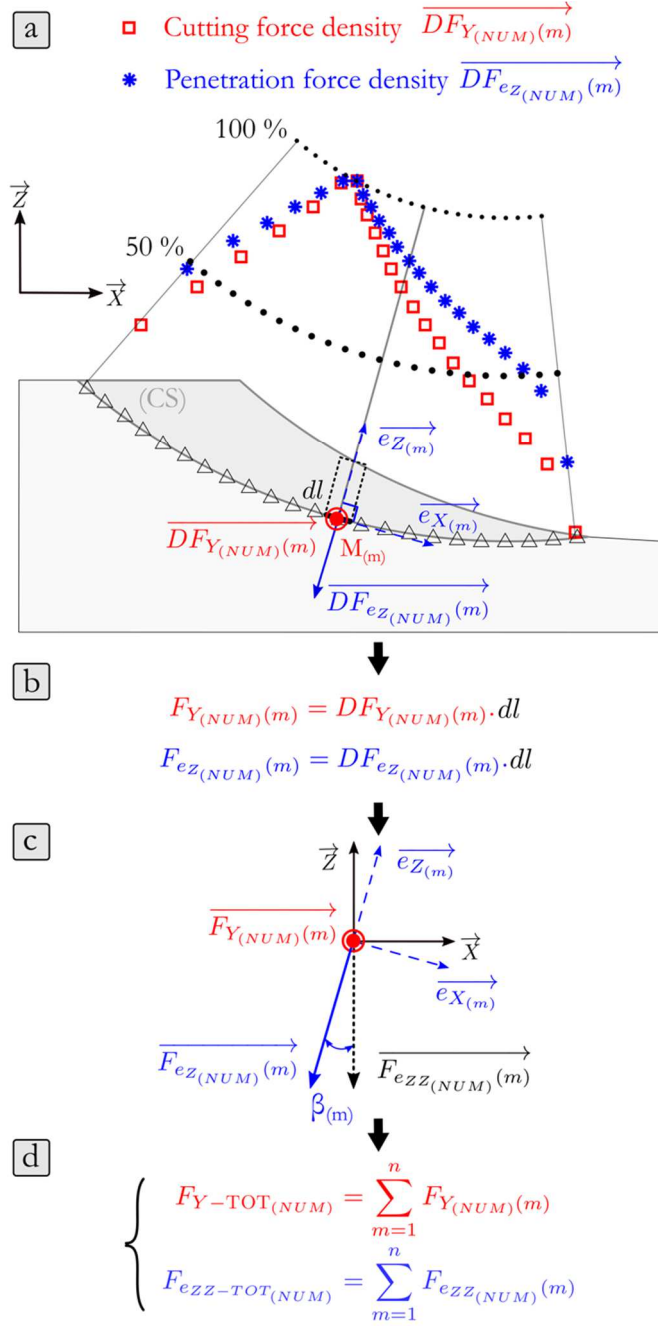
Fig. 8: Macroscopic numerical forces building given a cut section *CS* and forces distribution extracted from 2D ALE cutting models.

NB: It is important to remember that numerical and experimental macroscopic forces are defined in the main coordinates system $S_R = (O, X, Y, Z)$ (Fig. 8). For each section $S_{(i)}$, the elementary cutting force $DF_{Y(NUM)}(i)$ and elementary penetration force $DF_{ez(NUM)}(i)$ are determined in the coordinates system

$S_L = \left(M_{(i)}, \overrightarrow{e_X}, \overrightarrow{e_Y}, \overrightarrow{e_Z}\right)$ which is inclined by $\beta_{(m)}$ degrees to the main coordinates system $S_R = (O, X, Y, Z)$. So, the numerical macroscopic cutting force $F_{Y-TOT(NUM)}$ and penetration force $F_{ezZ-TOT(NUM)}$ are estimated by adding all the *n* elementary forces along the cutting edge after being transferred into the main coordinate system S_R thanks to equations 4, 5 and 6, with *n* being the number of sections to consider depending on the mesh size.

$$F_{ezZ(NUM)}(m) = \overrightarrow{F_{ez(NUM)}(m)} \cdot \overrightarrow{Z} = F_{ez(NUM)}(m) \cdot cos(\beta_{(m)}) \tag{4}$$

13

$$F_{eZZ-TOT_{(NUM)}} = \sum_{m=1}^{n} F_{eZZ_{(NUM)}}(m) \qquad (5)$$

$$F_{Y-TOT_{(NUM)}} = \sum_{m=1}^{n} F_{Y_{(NUM)}}(m) \qquad (6)$$

$$G_{F_Y} = \frac{F_{Y(EXP)}}{F_{Y-TOT_{(NUM)}}} \qquad G_{F_Z} = \frac{F_{Z(EXP)}}{F_{eZZ-TOT_{(NUM)}}}$$
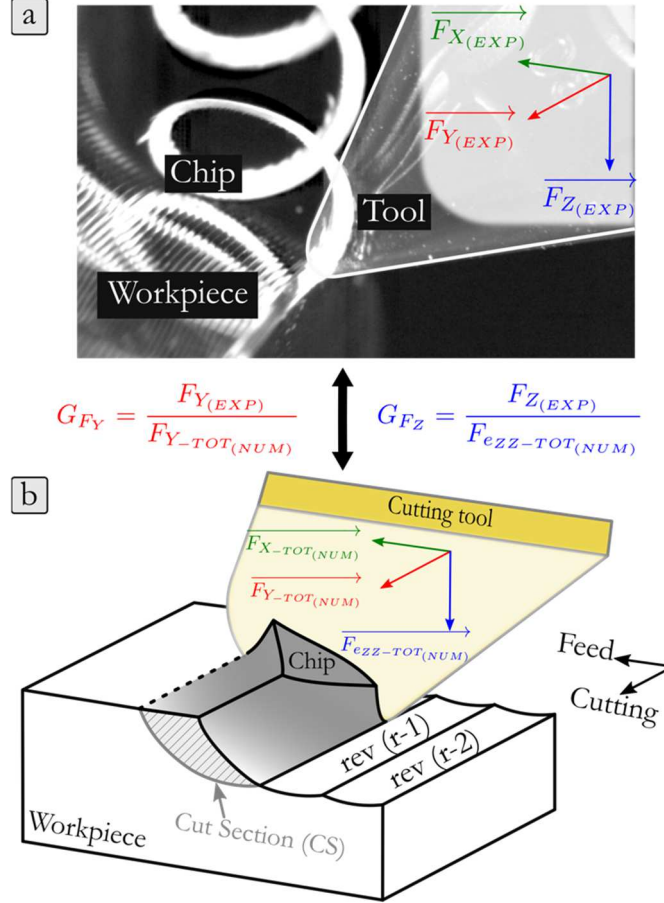
Fig. 9: Macroscopic forces correction factors introduction due to the comparison of macroscopic numerical (a) and experimental (b) forces measured throughout instrumented tests.

Based on the 3D macroscopic numerical cutting force $F_{Y-TOT(NUM)}$ and penetration force $F_{eZZ-TOT(NUM)}$ on the one hand and on the experimental cutting force $F_{Y(EXP)}$ and penetration force $F_{Z(EXP)}$ on the other hand, it becomes possible to adjust the magnitude of the equivalent thermomechanical loadings. The original work on the hybrid approach by Mondelin et al. (2012) has shown that the estimation of the heat flux distribution depends mainly on the cutting force component F_Y. So the heat flux density is calibrated thanks to the ratio G_{FY} between the experimental cutting force $F_{Y(EXP)}$ and the numerical cutting force $F_{Y-TOT(NUM)}$ (eq.7) (step corresponding to Fig. 3-5) as shown in Fig. 9. The tangential stress is also calibrated thanks to the ratio G_{FY} as this stress is oriented parallel to the cutting force component F_Y. The normal stress is calibrated thanks to the ratio G_{FZ} between the experimental penetration force $F_{Z(EXP)}$ and the numerical penetration force $F_{eZZ-TOT(NUM)}$ (eq.8), as this stress is oriented parallel to the penetration force component.

$$G_{F_Y} = \frac{F_{Y(EXP)}}{F_{Y-TOT_{(NUM)}}} \qquad (7)$$

$$G_{FZ} = \frac{F_{Z(EXP)}}{F_{e_{ZZ-TOT(NUM)}}}$$

(8)

Consequently, it is possible to assess the final 3D equivalent thermo-mechanical loadings based on equations 9, 10 and 11.

Heat flux density = $\varphi_{th-3D(calibrated)}$ = $G_{FY}.\varphi_{th-3D-appro}$ (9)

Normal pressure = $\sigma_{n-3D(calibrated)}$ = $G_{FZ}.\sigma_{n-3D-appro}$ (10)

Tangential pressure = $\sigma_{t-3D(calibrated)}$ = $G_{FY}.\sigma_{t-3D-appro}$ (11)

An example of thermo-mechanical loadings, corresponding to the case study presented in section 3, is illustrated in Fig. 10. It is important to highlight that this new method of calibration does not need as many experimental data as the one used by Mondelin et al. (2012): chip thickness, contact length on the flank face, etc... The new method only requires two forces components, which makes it much easier to apply.
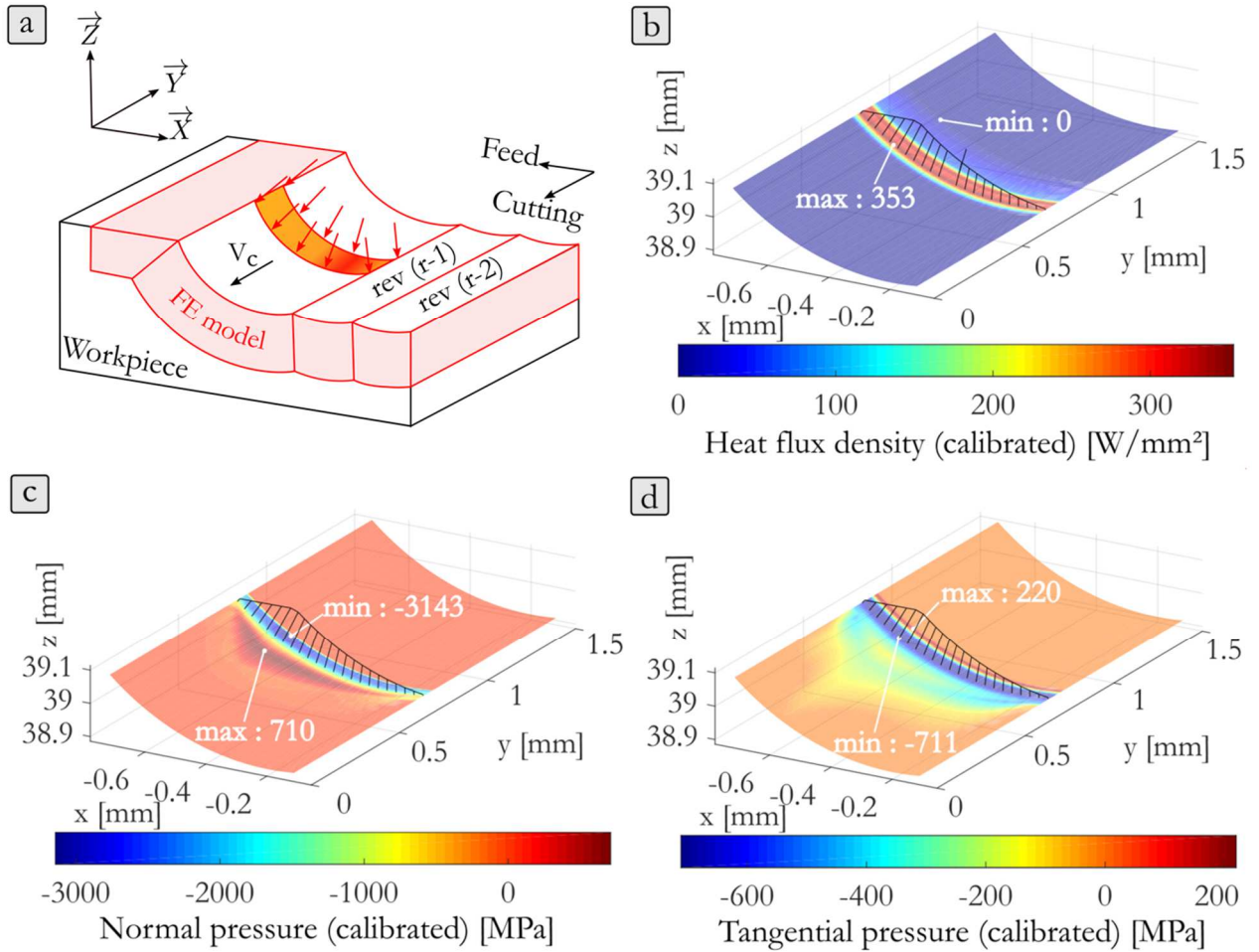

Fig. 10: Final 3D equivalent thermo-mechanical loadings description with physical shapes and corrected intensities. a) finite element model, b) heat flux density, c) normal pressure, d) tangential pressure.

2.4 Thermo-mechanical simulation (Residual stresses modelling)

The last step of the methodology (corresponding to Fig. 3-6) consists in applying the equivalent thermo-mechanical loadings on the grooved surface and to move it in the cutting direction with a velocity corresponding to the cutting speed V_c. The implicit finite element software SYSWELD ʀ is involved. Fig. 11 illustrates the finite element model including its dimensions and mesh sizes. Concerning the boundary conditions, all the faces are mechanically constrained blocking every node in the three directions except the above face where the equivalent thermo-mechanical loadings are applied. Heat transfers are also allowed to model the conduction phenomenon with the workpiece bulk and the heat exchange with the external environment (air, liquid...). This model enables the simulation of a single revolution (r). As stated by Mondelin et al. (2012), it is necessary to simulate several revolutions so as to obtain a steady state. Indeed, the thermo-mechanical loadings applied during the revolution (r) modify the residual stress state induced during the previous revolution ($r − 1$), ($r − 2$),... It is common to simulate 5 to 7 revolutions before reaching the steady state for the case study that will be presented in section 3.
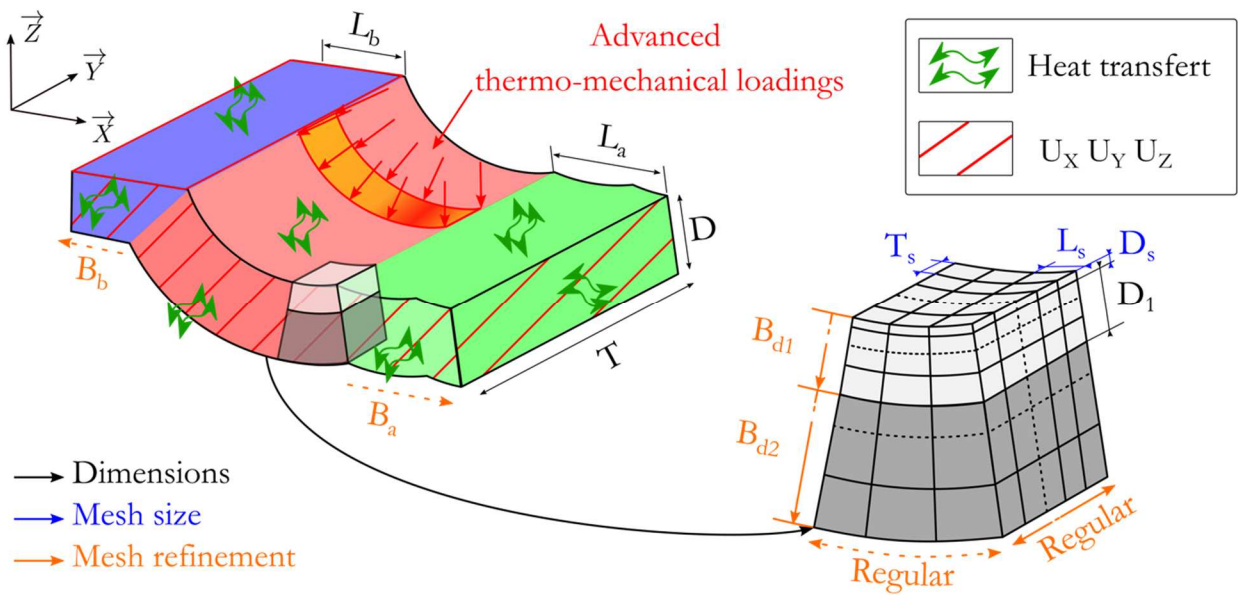
Fig. 11: Residual stresses thermo-mechanical model description. Illustration of the finite element mesh size, dimensions and boundary conditions.

NB: it is important to remember that this model considers an elementary volume of the real workpiece. So, after having simulated the movement of the thermo-mechanical loadings, it is mandatory to simulate the cooling phase. The cutting phase lasts during $t_{cutting}$ seconds (eq.12) whereas the cooling phase lasts $t_{cooling}$ seconds (eq.13). T is the model length (Fig. 11) and D is the workpiece diameter. Then the next revolution can be simulated and so on.

$$t_{cutting} = \frac{T}{V_c}$$

(12)

$$t_{cooling} = \frac{\pi D - T}{V_c}$$

(13)

As it is necessary to simulate several revolutions to reach a steady state, it becomes necessary to modify the model geometry between two revolutions due to the material removal. Fig. 12-a illustrates the geometrical model (red colour) when simulating the revolution (r). Then Fig. 12-b presents the updated geometry (blue colour) when simulating the revolution (r+1). As a consequence, it is necessary to transfer the residual stress fields generated after the previous geometry toward the new geometry

(initial residual stress field is present before the application of the thermo-mechanical loadings during revolution (r+1)). The numerical field transfer principle has already been presented by Kermouche et al. (2009).
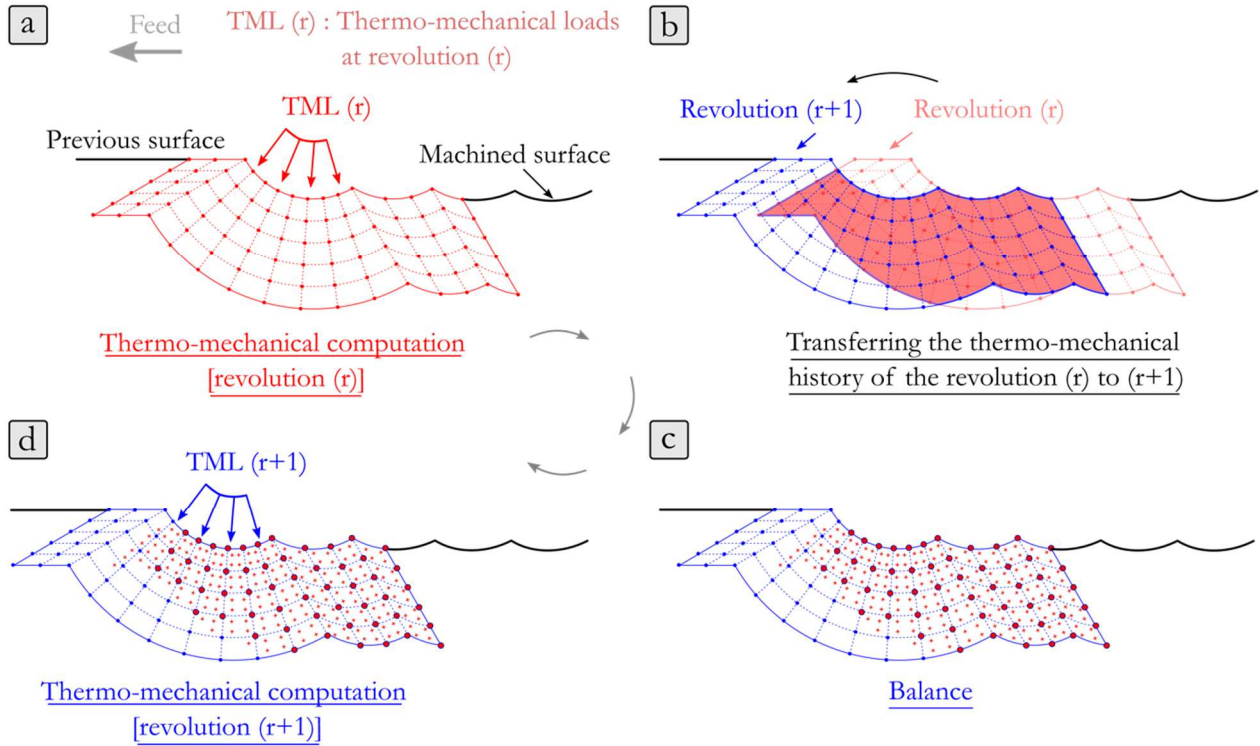
Fig. 12: Field transfer procedure used for the modelling of several cutting tool passages (i.e. several thermo-mechanical loadings sets onto the machined surface). a) thermo-mechanical computation at revolution (r), b) fields transfer from revolution (r) to (r+1), c) balance step, d) thermo-mechanical computation at revolution (r+1).

3 Validation of the new model on a case study

This section aims at applying the new modelling strategy on a case study corresponding to a longitudinal turning operation of a 15-5PH martensitic stainless steel. Moreover, the previous model one proposed by Mondelin et al. (2012) is also applied on the same case study. This will enable the evaluation of the improvements of the new modelling strategy.

3.1 Case-study and experimental results

Fig. 13-a shows the longitudinal turning operation. The cutting tool is a rhombic $TiCN - Al_2O_3$ coated carbide DNMG150608 PM 4325 insert (tool tip radius R_ϵ=0.8 mm, cutting edge radius R_β=70 μm) hold in a PDJNL2020K15 tool holder (cutting edge angle κ_r=93⁰). Concerning the tool micro-geometry, the working rake angle is observed to be γ = 1⁰, the clearance angle to α = 6⁰ and the inclination angle to λ_s = 0⁰. Regarding the cutting conditions, cutting speed V_c = 120 m/min, depth of cut a_p = 0.2 mm and feed f = 0.2 mm.rev⁻¹. Tests were performed in dry conditions.
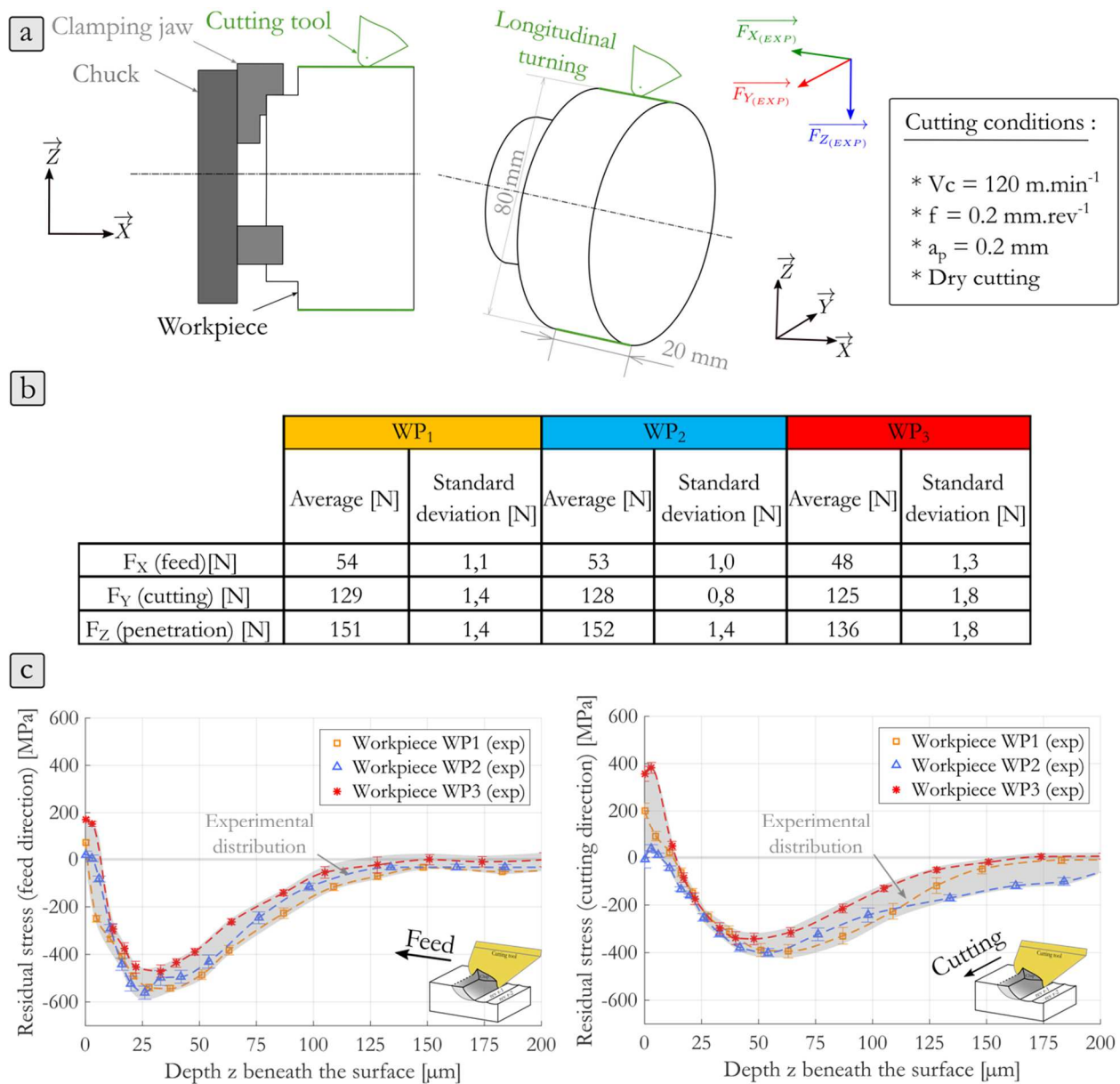
Fig. 13: Model validation experimental case description. a) case-study with cutting conditions, b) macroscopic experimental turning forces for three turning tests, c) residual stresses profiles beneath the surface in two directions.

Three instrumented turning tests (named from workpiece WP1 to WP3) have been replicated in such conditions. Macroscopic experimental cutting force $F_{Y(EXP)}$ and penetration force $F_{Z(EXP)}$ were measured during the machining thanks to a Kistler dynamometer (Fig. 9-a and Fig. 13-a). The average values and their deviation are presented in Fig. 13-b. Some limited variations can be observed. However, it remains within a reasonable range corresponding to common experimental deviations. Then, residual stresses were estimated by means of X-Ray diffraction with the same measuring conditions and set-up as described in Mondelin et al. (2012). The X-Ray beam has a diameter of 2 mm and its penetration depth is around 5 μm, that averages the experimental results within a volume. An electro-polishing technique was employed to remove material layer by layer and to rebuild the residual stress profile. The three corresponding residual stress signatures for the three workpieces are superposed in Fig. 13-c. They are analysed in two directions: feed and cutting directions. The profiles have a typical hook shape commonly observed after turning. They are consistent with the ones presented in Mondelin et al. (2012). Tensile stresses are present in the external layer, followed by a compressive valley. Finally, the profiles come

back to a near-zero stress. The affected depth is assessed to 100-125 μm. The three profiles exhibit small variations that are consistent with common experimental deviations. So as to consider the small variation between the three residual stress profiles, a grey cloud is plotted in Fig. 13-c. The same grey cloud will remain to compare these experimental results with the numerical results.

3.2   Numerical results

This section describes the input data used to compute the residual stress profiles.

3.2.1   2D ALE cutting modelling in ABAQUS Explicit

This section brings the input data corresponding to the steps 1 and 2 in Fig. 3. In this case-study, the uncut chip thickness is labelled $h_{(i)} \in$ [0 μm, 110 μm]. So as to limit the number of 2D orthogonal simulations, it is proposed to perform only four simulations with the following uncut chip thicknesses $h_{(1)}$=10 μm, $h_{(2)}$=40 μm, $h_{(3)}$=70 μm, $h_{(4)}$=110 μm. Intermediate values of $h_{(i)}$ are then interpolated later to predict 3D equivalent thermo-mechanical loadings. The thermophysical properties of the workmaterial and cutting tool carbide substrate are respectively described in Table 1 and Table 2. The friction model and the tool/workpiece heat partition model are dependent on the local sliding speed. They are presented in Table 3 since Mondelin et al. (2012). As the local sliding velocity vary along the workmaterial / cutting tool, friction and heat partition also vary along the workmaterial / cutting tool. In the present work, the sliding velocity can not exceed the cutting speed 120 m/min, so friction coefficient $\mu \in$ [0.25, 0.7] ±0.05 and heat partition coefficient $\lambda \in$ [13% - 25%] ±5%.

The thermal contact resistance at the tool/workpiece interface is equal to 10 000 [$W.m^2.K^{-1}$] as stated by Guillot et al. (2008). The Taylor-Quinney coefficient representing the plastic work fraction dissipated into heat is fixed to 0.9 as used in Afrasiabi et al. (2019). The simulation duration is set to 2 ms so as to reach a steady-state of the cutting and penetration forces and heat flux distribution along the extraction path.

Table 1: Thermophysical properties of the 15-5PH workmaterial.

Parameter	Temperature	Value
Thermal conductivity λ $[W.m\text{-}1.°C^{-1}]$ Fieldhouse and Lang (1961)	0	8.7
	1200	29.2
Specific heat C_p $[J.kg^{-1}.°C^{-1}]$ Fieldhouse and Lang (1961)	0	248
	1200	1400
Density ρ $[Kg.m^3]$ AkSteel (2017)	0	7810
	1200	7450
Young's Modulus E $[MPa]$ Department of defense (1998)	20	197 000
	1200	128 600
Thermal expansion coefficient α $[°C^{-1}]$ AkSteel (2017)	-73	0.0000104
	1200	0.0000145
Poisson's coefficient ν [-] AkSteel (2017)	-	0.272

Table 2: Thermophysical properties of the tool carbide substrate

Parameter	Value
Thermal conductivity K $[W.m\text{-}1.°C^{-1}]$	110
Specific heat C $[J.kg^{-1}.°C^{-1}]$	288
Density ρ $[Kg.m^3]$	14 600
Young's Modulus E $[MPa]$	620 000
Thermal expansion coefficient α $[°C^{-1}]$	0.0000049
Poisson's coefficient ν [-]	0.235

Table 3: Tribological properties of the couple 15−5*PH/*(*TiCN +Al*$_2$*O*$_3$) (*V*$_s$: local sliding speed) (Mondelin (2012)).

Friction coefficient μ [-]	$\mu = 2.12 V_s^{-0.45}$
Tool/workpiece heat partition coefficient λ [%]	$\lambda = 230 . V_s^{-0.6}$

A Johnson-Cook elastoviscoplastic formulation used by Mondelin et al. (2012) is also employed in this paper for the 2D ALE model. Table 4 gives the Johnson-Cook parameters useful for eq.14.

$$\sigma_{eq} = \left[A + B.\epsilon_p^n \right] . \left[1 + C.ln \left(\frac{\dot{\epsilon}_p}{\dot{\epsilon}_0} \right) \right] . \left[1 - \left(\frac{T - T_0}{T_m - T_0} \right)^m \right]$$

(14)

Where ϵ_p^n is the current plastic strain, $\dot{\epsilon}_p$ the plastic strain rate, $\dot{\epsilon}_O$ the reference plastic strain rate, A the yield strength, B the hardening modulus, n the hardening coefficient, C the strain rate sensitivity coefficient, m the thermal softening coefficient, T the current temperature, T_0 the room temperature and T_m the melting temperature. From a rheological point of view, three terms can be distinguished in the equation: the first one represents the elastoplasticity, the second the viscosity, and the third the softening effect.

Table 4: Flow stress model - Johnson-Cook model parameters for 15-5PH (Mondelin et al. (2012)).

A [MPa]	B [MPa]	n	C	$\dot{\varepsilon}_O$	m	T_m [°C]	T_0 [°C]
855	448	0.14	0.0137	1	0.63	1440	20

3.2.2   Calibration of the 3D thermomechanical loadings

This section brings the input data corresponding to the steps 3 and 5 in Fig. 3. First, the experimental force measurements already presented in Fig. 13 are reported in Tab. 5. Then the numerical forces are calculated based on the methodology described in section 2.3. Finally the calibration ratio G_{FY} and G_{Fz} are calculated thanks to equations 7 and 8. Table 5 shows first that the two calibration ratios differ amongst the experimental tests (natural experimental deviation). Second, it confirms that the calibration ratio corresponding to the penetration force FZ is higher than the one corresponding to the cutting force, because of the weaknesses of ALE models discussed in section .

Table 5: Comparison between the experimental forces measurements and the predicted forces – Calculation of the corresponding calibration factor GFY and GFZ for each experimental test.

	WP1				WP2				WP3			
	Exp.	Num	G_{FY}	G_{FZ}	Exp.	Num	G_{FY}	G_{FZ}	Exp.	Num	G_{FY}	G_{FZ}
F_Y (cutting) (N)	129	91	1.42		128	91	1.41		125	91	1.37	
F_Z (penetration) (N)	151	87		1.74	152	87		1.75	136	87		1.56

3.2.3   3D residual stress modelling in SYSWELD

This section brings the input data corresponding to the step 5 in Fig. 3. The cutting edge is discretized into sections having a width of dl = 30 μm. This also determines the mesh size L_s. The parameters of the finite element model are described in Table 6.

Table 6: 3D mesh parameters corresponding to Fig. 11.

Dimensions [mm]	L_a	L_b	D	T
	0.8	0.2	1	1.5
Mesh size [mm]	L_s	D_s	T_s	D_1
	0.03	0.003	0.0125	0.250
Mesh refinement [-]	B_a	B_b	B_{d1}	B_{d2}
	1	1	1.4	1.6

The same thermophysical properties of the workmaterial as those used for the ALE cutting model are implemented in SYSWELD. In addition, a heat exchange coefficient air/workpiece is fixed to 500 $W.m^{-2}.C^{-1}$ as in Mondelin et al. (2012). The model can also transfer heat towards the bulk of the workpiece with a heat exchange coefficient set to 2000 $W.m^{-2}.C^{-1}$. The flow stress model differs from the ALE cutting model as several revolutions have to be modelled. As a consequence, the machined surface has to withstand cyclic thermo-mechanical loadings/unloadings. A von Mises elastoplastic behaviour (eq.15) associated with an Armstrong-Frederick kinematic hardening (eq.16), as determined by Mondelin (2012) from cycling tests, is thus implemented. Table 7 gives the required parameters for implementing the corresponding model.

$$f = \sqrt{3J_2(\bar{\bar{\sigma}} - \bar{\bar{\chi}})} - \sigma_y \quad (15)$$

$$\dot{\bar{\bar{\chi}}} = \frac{2}{3}C\dot{\bar{\bar{\epsilon}}}^p - \gamma\bar{\bar{\chi}}\dot{p} \quad (16)$$

where C and γ are the workmaterial parameters, σ_y the yield strength and p the cumulative plastic strain defined in equation 17

$$\dot{p} = \sqrt{\frac{2}{3}\dot{\bar{\bar{\epsilon}}}^p : \dot{\bar{\bar{\epsilon}}}^p} \quad (17)$$

Table 7: Flow Stress model - Armstrong-Frederick kinematic hardening law parameters for 15-5PH (Mondelin (2012)).

Temperature [°C]	σ_y [MPa]	C	γ
20	530	421405	730
300	382	284420	508

600	197	120000	600

3.3   Comparison of residual stress profiles

Based on the previous input data, it becomes possible to run 3D simulation in SYSWELD and by the way to estimate residual stress profiles. As three experiments have been conducted, three sets of forces have been measured (Fig. 13-b). As a consequence, the hybrid approach necessitates to run one simulation for each set of measured forces (one thermo-mechanical loadings calibration for one set of experimental force values). So, three simulations with three different thermo-mechanical loadings have been launched. The computation time for simulating 7 revolutions is reasonable: 24 hours with a 3.2 GHz processor (4 cores). This brings hope for industrial use of this new method. Fig. 14-b illustrates residual stresses variation along the machined surface with a period corresponding to the feed (f = 0.2 mm.rev^{-1}) which is well known since the work of Mondelin et al. (2012). On the contrary, the X-Ray beam averages the residual stress estimation within a much larger volume (diameter 2 mm of the X-Ray beam and penetration depth of 5 μm). So it is necessary to average as well numerical results within a similar volume as well in order to compare numerical and experimental results on the surface. Experimental values of residual stresses have been estimated for several depths below the surface thanks to an electro-polishing technique. For each depth, numerical residual stresses were also averaged so as to estimate a single residual stress value at a corresponding depth beneath the surface. All the averaged values provide the numerical residual stress profile (Fig. 14-c).
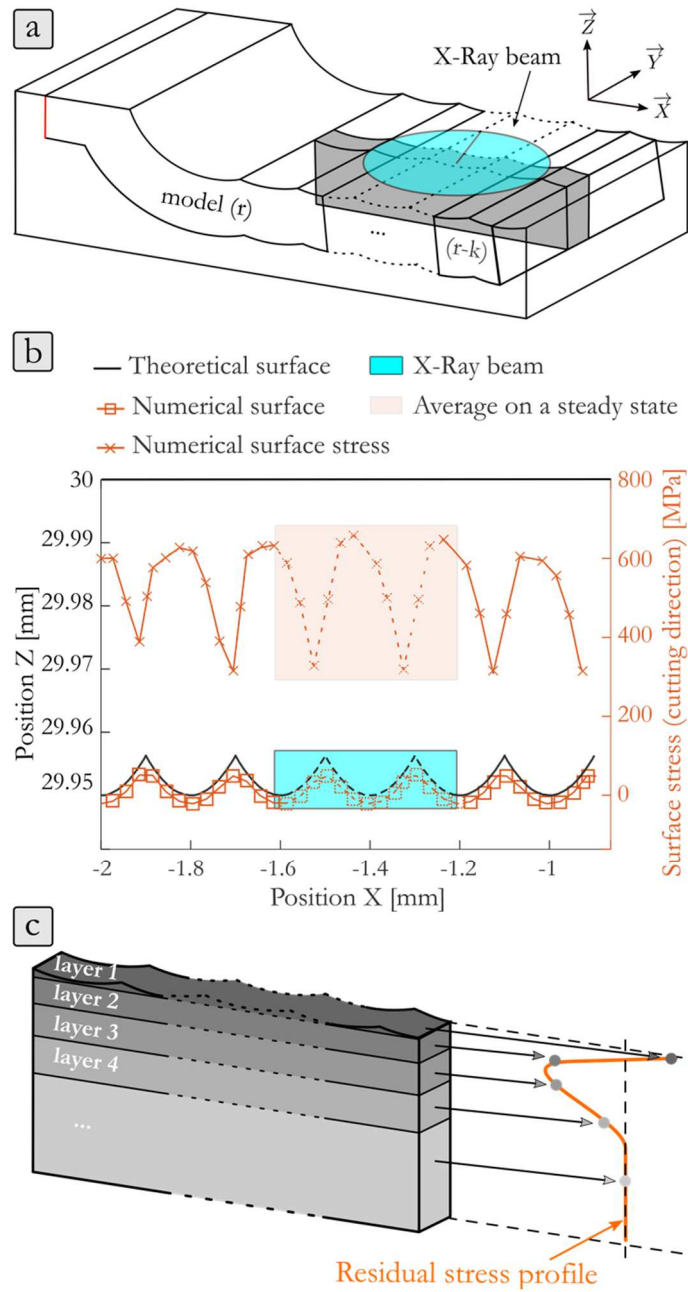
Fig. 14: Numerical residual stress profiles building methodology, a) model overlapping of successive revolutions, b) surface residual stress average on a stabilised zone, c) in-depth average layer by layer for residual stress profile building.
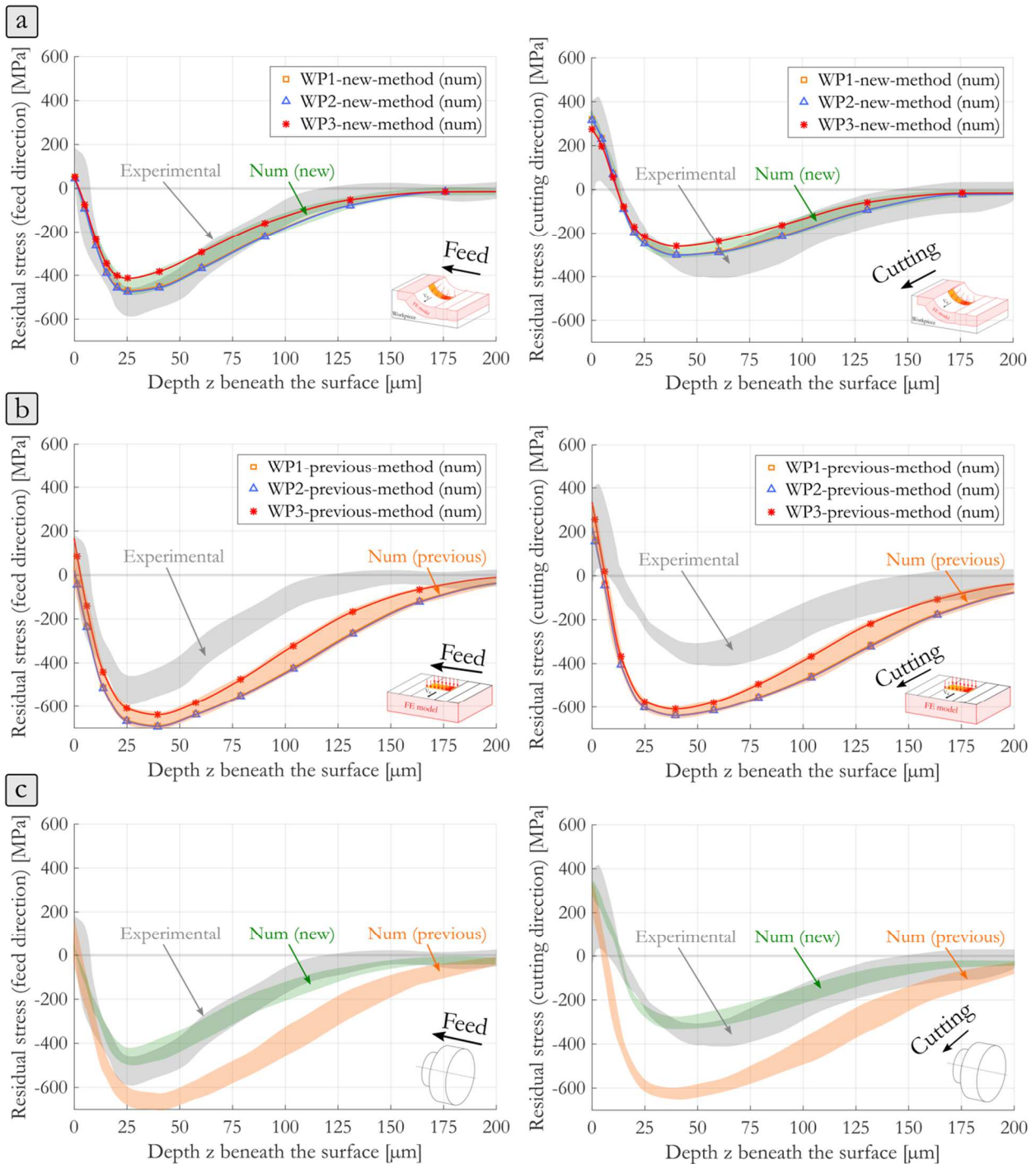
Fig. 15: Residual stress comparison for numerical model validation, experimental results are displayed through the grey cloud and compared for the three workpieces with a) the new numerical predictions, b) the previous numerical predictions, c) overview of the accuracy of both numerical methods predictions compared to the experimental results.

Fig. 15 presents the residual stress profiles predicted thanks to the new model (Fig. 15-a). Based on the three simulations corresponding to the three sets of experimental forces, three residual stress profiles are computed. The three numerical profiles are included within a green cloud. By comparing the experimental residual stress profiles (grey cloud), it appears that the model predicts residual stress profiles with a good accuracy in both directions (cutting and feed directions). It is only possible to observe a little under-estimation of the intensity of the compression valley in both directions. This result, obtained in a single case study, is promising. However, it is necessary to keep in mind that several input

parameters are involved in the model (flow stress model, friction model, thermal properties, ….). A sensitivity study may be of interest so as to identify the most critical input parameters.

As this new model differs significantly from the previous model published by Mondelin et al. (2012), Fig. 15-b plots the numerical results obtained with this previous model. Once again, three simulations have been launched corresponding to the three sets of experimental forces. The three curves are included within an orange cloud. It is not surprising to observe that the predicted residual stresses exhibits the same hooked residual stress profiles. The results are not that accurate, especially in the cutting direction, with a difference that can reach 300 MPa compared to experimental values. When comparing the three clouds in Fig. 15-c (grey: experimental values, green: new model, orange: previous model), it is clear that the new model is more accurate, especially for the first 50 μm where crack initiation is likely to occur for the 15-5PH steel. Hence, this new modelling strategy brings a clear improvement of the 3D hybrid approach to predict residual stresses, by considering a more realistic surface topography, and by modelling more accurate and fine thermo-mechanical loadings.

4   Conclusions

This paper has presented an original modeling strategy to predict residual stress fields induced by a longitudinal turning operation. This new method is based on the numerical modelling of equivalent thermo-mechanical loadings applied on a surface instead of modelling the whole 3D material removal with a complex chip geometry. Several revolutions are modelled until reaching a steady state. This new method is an improvement of a previous one. The main improvement comes first from a much finer way to model the 3D thermo-mechanical loadings thanks to several 2D orthogonal cutting simulations for each sub-section. Hence, the machined surface considers a more realistic surface topography by taking into account the surface roughness. Finally, this method is much easier to handle as the calibration of the thermo-mechanical loadings only requires measuring the cutting and penetration forces, that are easily accessible for an end-user. This new method provides much more accurate residual stress fields within a reasonable computation duration, that makes it promising for industrial use. Moreover, it has the potential to model more complex cutting tools by taking into account the variation of their local geometry along the cutting edge, and by considering more complex trajectories by investigating various cut sections. With such capabilities, this method could be applied for the modelling of other metal cutting processes.

Acknowledgments

References

Afrasiabi, M., Roethlin, M., Klippel, H., Wegener, K., 2019. Meshfree simulation of metal cutting: an updated lagrangian approach with dynamic refinement. International Journal of Mechanical Sciences 160, 451–466. doi:10.1016/j.ijmecsci.2019.06.045.

AkSteel, 2017. Product data bulletin - 15-5PH Stainless steel. AKSteel.

Attanasio, A., Ceretti, E., Giardini, C., 2009. 3D FE modelling of superficial residual stresses in turning operations. Machining Science and Technology 13, 317–337. doi:10.1080/ 10910340903237806.

Courbon, C., Mabrouki, T., Rech, J., Mazuyer, D., Perrard, F., D'Eramo, E., 2014. Further insight into the chip formation of ferritic-pearlitic steels: Microstructural evolutions and associated thermo-mechanical loadings. International Journal of Machine Tools and Manufacture 77, 34–46. doi:10.1016/j.ijmachtools.2013.10.010.

Davim, J., 2008. Machining-Fundamentals and Recent advances. Springer London. doi:10.1007/ 978-1-84800-213-5.

Department of defense, U., 1998. Military Handbook - metallic materials and elements for aerospace vehicle structures - MIL-HDBK-5H.

Ee, K., Dillon, O., Jawahir, I., 2005. Finite element modeling of residual stresses in machining induced by cutting using a tool with finite edge radius. International Journal of Mechanical Sciences 47, 1611–1628. doi:10.1016/j.ijmecsci.2005.06.001.

Fieldhouse, I., Lang, J., 1961. Measurement of Thermal Properties - WADD technical report 60-904. Technical Report. Armour Research Foudation.

Griffiths, B., 1971, Manufacturing surface technology – surface integrity and functional performance, Penton Press London, ISBN18571-8029-1.

Guillot, E., Bourouga, B., Garnier, B., Dubar, L., 2008. Estimation of thermal contact parameters at a worpiece-tool interface in a hsm process. International Journal of Material Forming 1, 1031– 1034. doi:10.1007/s12289-008-0194-x.

Guo, Y., Warren, A., Hashimoto, F., 2010. The basic relationships between residual stress, white layer, and fatigue life of hard turned and ground surfaces in rolling contact. CIRP Journal of Manufacturing Science and Technology 2, 129–134. doi:10.1016/j.cirpj.2009.12.002.

Guo, Y.B, Liu, C.R., 2002, FEM analysis of mechanical state on sequentially machined surfaces. Machining Science andTechnology 6/1:21-41. doi.org/10.1081/MST-120003183.

Kermouche, G., Aleksy, N., Loubet, J., Bergheau, J., 2009. Finite element modeling of the scratch response of a coated time-dependent solid. Wear 267, 1945–1953. doi:10.1016/j.wear.2009.05. 005.

Liu, C.R., Guo, Y., 2000. Finite element analysis of the effect of sequential cuts and tool-chip friction on residual stresses in a machined layer. International Journal of Mechanical Sciences 42, 1069–1086. doi:10.1016/S0020-7403(99)00042-9.

Mondelin, A., Valiorgue, F., Rech, J., Coret, M., Feulvarch, E., 2012. Hybrid model for the prediction of residual stresses induced by 15-5PH steel turning. International Journal of Mechanical Sciences 58, 69–85. doi:10.1016/j.ijmecsci.2012.03.003.

Nasr, M.N., Ng, E.G., Elbestawi, M., 2007. Modelling the effects of tool-edge radius on residual stresses when orthogonal cutting AISI 316l. International Journal of Machine Tools and Manufacture 47, 401–411. doi:10.1016/j.ijmachtools.2006.03.004.

Paulo Davim, J., 2008, Machining : fundamentals and recent advances, Springer, ISBN 978-1-84800-212-8.

Shet, C., Deng, X., 2003. Residual stresses and strains in orthogonal metal cutting. International Journal of Machine Tools and Manufacture 43, 573–587. doi:10.1016/S0890-6955(03)00018-X.

Smith, S., Melkote, S.N., Lara-Curzio, E., Watkins, T.R., Allard, L., Riester, L., 2007. Effect of surface integrity of hard turned AISI 52100 steel on fatigue performance. Materials Science and Engineering: A 459, 337–346. doi:10.1016/j.msea.2007.01.011.

Ulutan, D., Ozel, T., 2011. Machining induced surface integrity in titanium and nickel alloys: A review. International Journal of Machine Tools and Manufacture 51, 250–280. doi:10.1016/j.ijmachtools.2010.11.003.